Compact topological edge modes through hybrid coupling of orbital angular momentum modes

Yang Wang,[1] Chuang Jiang,[2] Miaomiao Zhao,[1,*] Dong Zhao,[2] and Shaolin Ke[2,†]
[1]*School of Electrical and Information Engineering, Hubei University of Science and Technology, Xianning 437100, China*
[2]*Hubei Key Laboratory of Optical Information and Pattern Recognition, Wuhan Institute of Technology, Wuhan 430205, China*

(Received 15 January 2024; revised 22 April 2024; accepted 28 May 2024; published 17 June 2024)

Topological waveguide arrays, which support robust light propagation through edge modes, offer a promising solution for fault-tolerant photonic chips. However, these arrays commonly require a considerable number of waveguide elements to ensure their topological protection, leading to increased footprint and fabrication costs. Here, we propose a topological waveguide array with only a few cells based on a photonic Aharonov-Bohm (AB) cage. This design is advantageous because the edge modes become compactly localized at the boundary waveguides. We achieve this by utilizing the orbital hybridization of the fundamental mode and first-order orbital angular momentum (OAM) modes to construct the AB cage, where arbitrary flux of artificial gauge fields (AGFs) can be generated and controlled by adjusting the angle between adjacent waveguides. Notably, these edge modes exhibit robustness against disorders of on-site potential and coupling, even within a small lattice. Furthermore, we demonstrate the extension of this mechanism to high-order OAM modes. Our work paves the way for miniaturizing topological devices using the orbital degree of freedom, holding the potential for exploring other AGF-enriched phenomena.

DOI: 10.1103/PhysRevA.109.063516

I. INTRODUCTION

Photonic integrated circuits are essential for optical interconnects, processing, and computing [1]. The performance of traditional optical components, such as waveguide couplers and resonators, heavily relies on local structural parameters. Minor changes in the spatial separation between two waveguides or resonators substantially impact the splitting ratio and working bandwidth. In addition, fabrication imperfections and disorders may destroy the function of devices. To meet these challenges, the field of topological photonics has emerged, using the topological degree of freedom that characterizes the global features of the wave function across the entire Brillouin zone [2–7]. This approach holds promise for the development of fault-tolerant photonic devices. Applications ranging from delay lines [8], broadband wave splitters and routers [9], sharply bended waveguiding [10], to high-performance lasers [11] have been proposed based on photonic crystals, metamaterials, split resonators, and more [12,13]. Photonic waveguide arrays, serving as the fundamental building blocks for integrated photonics, have garnered considerable attention in exploring topological phenomena [14–16]. The topological Su-Schrieffer-Heeger (SSH) model [17], Floquet topological insulators [18–20], and high-order topological insulators [21] were explored in the straight or helical waveguides. These waveguides support edge or corner modes at the boundary or interface, contributing to their fault-tolerant characteristics. However, the topological modes arising from the bulk nature of waveguide arrays commonly require many elements to ensure their topological protection, resulting in large sizes and high fabrication expenses. To address this challenge, various strategies, such as twisted edge bands [22], twig boundaries [23], parity-time symmetry [24], and non-Hermitian coupling [25], have been proposed to decrease the mode coupling of topological modes at different boundaries, thereby reducing the system size. Here, we introduce another mechanism by employing an artificial gauge field (AGF) to achieve this goal.

Artificial gauge fields for photons mimic the interaction of electromagnetic fields with charged particles. They offer an alternative way for controlling light propagation [26–29]. Examples include Bloch oscillation, dynamical localization, and negative refraction [28,30]. The physical origin of AGFs is understood by the Aharonov-Bohm (AB) effect, where the phase factor of the wave function acquired along a closed loop is gauge invariant [31]. Consequently, an AGF can be generated by engineering the geometry of systems or applying external modulation to induce a nonreciprocal phase in the wave tunneling process. For instance, electro-optic modulation imposed on waveguides or resonators introduces a nonreciprocal phase shift, acting as AGFs between two frequency channels [27]. Using auxiliary rings between two site rings, the difference of propagation length gives rise to AGFs as well [32]. The orbital degree of freedom has also been exploited to realize AGFs, thanks to the nonuniform phase distributions of high-order modes [33–40]. Mode interference and hybrid coupling between s, p, and d orbital modes were reported to generate π gauge flux, which can be utilized in photonic Aharonov-Bohm (AB) cages [34,41–45], quadrupole topological insulators [37], Möbius topological insulators [33,36,46], and coherent control of topological edge modes [47]. The orbital degree of freedom is also used to create synthetic dimensions, allowing the

*Contact author: miaomiaozhao@hbust.edu.cn
†Contact author: keshaolin@wit.edu.cn

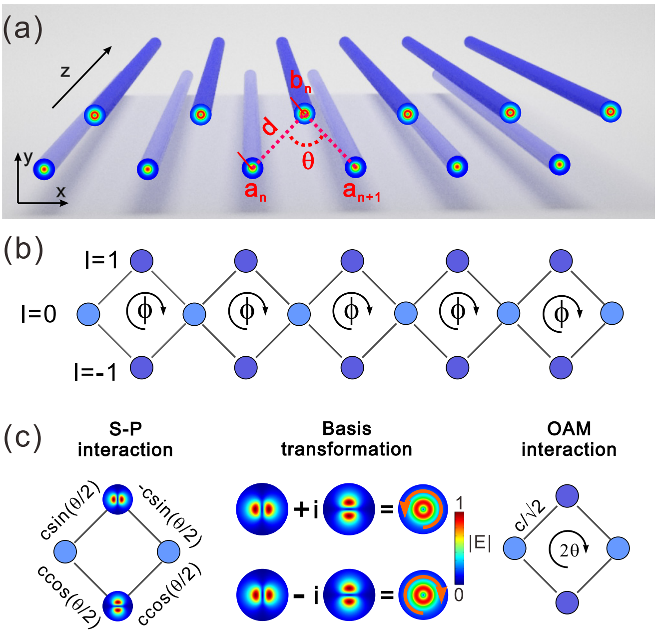

FIG. 1. Arbitrary gauge flux and photonic AB cage induced by orbital hybridization. (a) Schematic of the proposed zigzag waveguide arrays carrying different OAM modes. (b) The effective tight-binding lattice for OAM modes with each plaquette filled with flux ϕ. (c) The coupling mechanism in $s-p$ modes and OAM modes, which are connected by a basis transformation.

exploration of rich topological phases that are not easily realized in spatial dimensions [48–50].

In this work, we show another opportunity offered by orbital-induced AGFs, effectively reducing the size of a waveguide array while preserving the topological edge modes. The proposed array consists of two different waveguide elements, supporting fundamental and first-order orbital angular momentum (OAM) modes, respectively. Their hybrid coupling gives rise to AGFs with arbitrary flux, tunable by the central angle of adjacent waveguides. Destructive interference leads to AB cages and compact topological edge modes. These modes form a compact platform and are localized only at boundary waveguides, unlike conventional topological modes, which exhibit exponential localization and are confined to many lattice sites. This approach effectively minimizes mode coupling at opposite boundaries when the waveguide elements are reduced in number. We present a comprehensive discussion of the robustness and the hybrid coupling of higher-order OAM modes. Our findings are important for minimizing the size of topological waveguide arrays. The utilization of orbital hybridization addresses the challenge to generate arbitrary gauge fields in straight waveguides.

II. ORBITAL HYBRIDIZATION INDUCED AGFS AND AB CAGING

The proposed waveguide array is arranged in a zigzag lattice, forming a triangle structure with a central angle denoted by θ, as shown in Fig. 1(a). The nth unit cell consists of two types of cylindrical waveguides, labelled as a_n for the fundamental mode ($l = 0$) and b_n for the first-order OAM modes ($l = \pm 1$). The refractive index of the $\mathrm{OAM}_{\pm 1}$ waveguide is higher than that of the OAM_0 waveguide, ensuring that their effective refractive indices are matched. The OAM modes display distinct ring-shaped and helical phase wave fronts, as described by [51–53]

$$\psi_n^{\pm l}(r,\varphi,z) = \psi_n^l(r)e^{\pm il(\varphi-\varphi_0)}e^{-i\beta_l z}, \tag{1}$$

where $\pm l$ represents the charge value, $\psi_n^1(r)$ is the radial field distribution of the nth waveguide, β_l signifies the propagation constant along the z direction, (r,φ) are polar coordinates, and φ_0 is an arbitrary phase origin. The separation d between any two neighboring waveguides is uniform, distinguished from conventional topological waveguide arrays with alternating short and long separations [17]. The coupling coefficient integrates the two mode profiles at adjacent waveguides. Considering the phase variation of $\mathrm{OAM}_{\pm 1}$ modes along the azimuthal angle, the mixed coupling of the two OAM modes naturally acquires a phase factor, serving as AGFs and forming the basis for topological edge modes. Specifically, assuming the phase origin φ_0 along the x direction, the coupling $c_{0,\pm 1}$ along the a_n to b_n path is $c/\sqrt{2}\exp[\mp i(\pi/2-\theta/2)]$, with the phase factor determined by the central angle of the triangle. The coupling $c_{\pm 1,0}$ along the b_n to a_{n+1} path has a phase factor $\pm(\pi/2+\theta/2)$ [35,54]. The effective tight-binding lattice for OAM modes, depicted in Fig. 1(b), exhibits a rhombic lattice where each plaquette experiences a gauge flux with $\phi = 2\theta$. For simplicity, the Bloch Hamiltonian of the orbital waveguide array is expressed

$$H(k) = \frac{c}{\sqrt{2}}\begin{pmatrix} 0 & e^{-i\phi/2}+e^{-ikd} & e^{i\phi/2}+e^{-ikd} \\ e^{i\phi/2}+e^{ikd} & 0 & 0 \\ e^{-i\phi/2}+e^{ikd} & 0 & 0 \end{pmatrix}, \tag{2}$$

where k represents the Bloch momentum. Three band structures are derived as

$$E(k) = 0, \pm\sqrt{2}c\sqrt{1+\cos(\phi/2)\cos(kd)}. \tag{3}$$

When $\phi = \pi$, the AB caging effect emerges due to the destructive interference between the two legs of the rhombus. In this scenario, the corresponding eigenmodes become compact, and all energy bands flatten across the entire Brillouin zone [26].

The generation of gauge flux is also verified through the transformation from $s-p$ coupling, illustrated in Fig. 1(c). Assuming a coupling coefficient between the s mode and a horizontal p mode is c and considering a plaquette of zigzag chain (three waveguides) as an example, the Hamiltonian in the $s-p$ basis is expressed as follows:

$$H_{sp} = c\begin{pmatrix} 0 & \sin(\theta/2) & \cos(\theta/2) & 0 \\ \sin(\theta/2) & 0 & 0 & -\sin(\theta/2) \\ \cos(\theta/2) & 0 & 0 & \cos(\theta/2) \\ 0 & -\sin(\theta/2) & \cos(\theta/2) & 0 \end{pmatrix}. \tag{4}$$

OAM modes can be synthesized through a combination of p_x and p_y modes according to [55]

$$\begin{pmatrix}\psi_{OAM_{+1}}\\ \psi_{OAM_{-1}}\end{pmatrix} = T_1\begin{pmatrix}\psi_{p_x}\\ \psi_{p_y}\end{pmatrix} = \frac{1}{\sqrt{2}}\begin{pmatrix}1 & i\\ 1 & -i\end{pmatrix}\begin{pmatrix}\psi_{p_x}\\ \psi_{p_y}\end{pmatrix}. \quad (5)$$

Then, by a transformation, the Hamiltonian in the basis of OAM modes is

$$\begin{aligned} H_{\mathrm{OAM}} &= T_2 H_{sp} T_2^{-1}\\ &= \frac{c}{\sqrt{2}}\begin{pmatrix} 0 & e^{-i\varphi_1} & e^{i\varphi_1} & 0\\ e^{i\varphi_1} & 0 & 0 & e^{i(\varphi_1+\theta)}\\ e^{-i\varphi_1} & 0 & 0 & e^{-i(\varphi_1+\theta)}\\ 0 & e^{-i(\varphi_1+\theta)} & e^{i(\varphi_1+\theta)} & 0\end{pmatrix}, \; T_2\\ &= \begin{pmatrix} 1 & 0 & 0 & 0\\ 0 & 1/\sqrt{2} & i/\sqrt{2} & 0\\ 0 & 1/\sqrt{2} & -i/\sqrt{2} & 0\\ 0 & 0 & 0 & 1\end{pmatrix}, \end{aligned} \quad (6)$$

where $\varphi_1 = \pi/2 - \theta/2$ represents the phase factor of the coupling $c_{0,\pm1}$ introduced along the a_n to b_n path. Nonreciprocal phase factors manifest in the coupling coefficient, and the accumulated phase along a closed loop should be $\phi = 2\theta$, acting as AGFs and effectively creating magnetic fields. Following this mechanism, we can construct AB chains with arbitrary gauge flux threading each plaquette, as shown in Fig. 1(b).

Orbital-induced AGFs have been observed in several studies. However, mixed couplings, such as $s-p$ or $s-d$ orbital couplings, are limited to creating a π flux [34,36]. In contrast, using the same order $\mathrm{OAM}_{\pm1}$ mode shows potential for generating arbitrary flux [35,38]. Nevertheless, challenges remain in creating an effective model that accounts for cross coupling between different circulation modes, and the precise determination of the flux value in each plaquette remains unclear. The condition for the AB caging phenomenon is highly critical, only satisfied for large separation such that the self- and cross couplings between adjusted OAM modes are the same. Unfortunately, meeting this condition results in a long propagation length. In Ref. [33], simulations indicate that a flat band is achieved when $d = 15\mu$m. In our work, the separation is $d = 7\mu$m, which is approximately half the separation used in the previous work. Our proposed scheme, involving the hybridization of two OAM modes, offers two distinct advantages. First, it enables the generation of arbitrary gauge flux in each plaquette, overcoming the limitation utilizing the same-order $\mathrm{OAM}_{\pm1}$ mode. Second, direct coupling between adjacent waveguides is used, without inserting auxiliary waveguides between two main ones. Consequently, the total length of the waveguides can be significantly reduced [56]. This approach differs from that of [38]. While both works utilize OAM modes to create gauge fields and topological bound modes, here we utilize hybrid coupling of OAM_0 and $\mathrm{OAM}_{\pm1}$, contrasting with [38], where all waveguides are the same, supporting $\mathrm{OAM}_{\pm1}$. The effective lattice is the Creutz ladder in [38], and the discussion mainly focuses on how the gauge fields affect topological phases. In contrast, in this work, the effective lattice is rhombic, aimed at creating flat bands and compact topological edge modes. Furthermore, in Sec. IV, we propose that high-order OAM modes can also be utilized to create gauge flux.

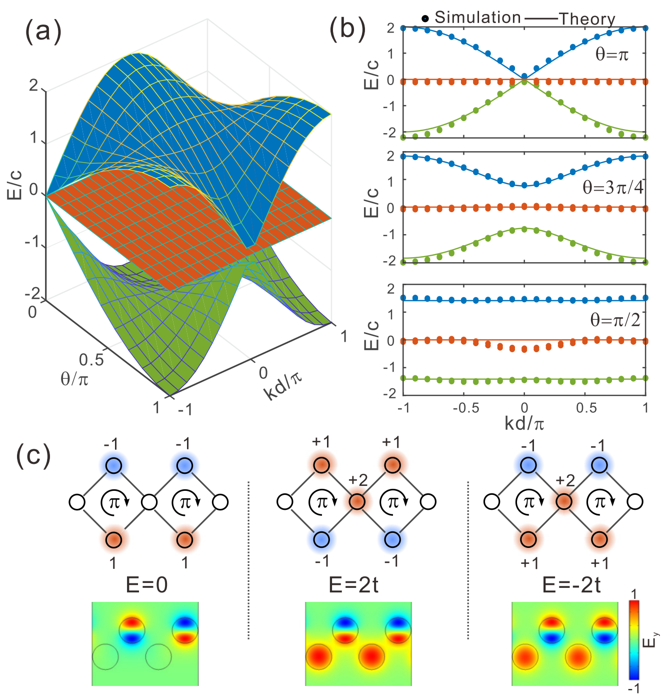

FIG. 2. Band structure and distribution of eigenmodes for AB cages. (a) Eigenenergy E as a function of Bloch momentum kd and central angle θ. (b) Theoretical (dots) and simulated (lines) band structures for three different central angles. The AB caging phenomenon emerges at $\theta = \pi/2$ as all bands become flat. (c) Theoretical (first row) and simulated (second row) amplitude distribution of bulk modes for three flat bands at $k = 0$.

Figure 2(a) illustrates the eigenenergy E for a system with periodic boundary as a function of Bloch momentum k and central angle θ. Three bands $E(k)$ are observed, with two generally dispersive bands and a middle flat band. As $\theta = \pi/2$, corresponding to flux $\phi = \pi$, the AB caging effect arises due to the destructive interference, causing all three bands to be flat. We conducted a full-wave simulation using COMSOL. In the simulation, a unit cell is used for mode analysis. The left and right edges are set as periodic conditions with a wave vector k along the x direction, while the top and bottom edges are scattering boundary conditions to absorb outgoing waves. The mesh is smaller than 1/5 of the effective wavelength. Subsequently, we sweep the Bloch wave vector k and solve for the effective index n_{eff} of supermodes. In the waveguides with the same parameters, the effective refractive index of $\mathrm{OAM}_{\pm1}$ is smaller than that of OAM_0. By increasing the refractive index of the $\mathrm{OAM}_{\pm1}$ waveguide, the effective refractive index can match that of the OAM_0 waveguide. The refractive indices of two waveguides in each cell are given by $n_0 = 1.5443$ for a_n and $n_1 = 1.5480$ for b_n, both with a radius $r = 2.4\mu$m. The cladding refractive index is $n_b = 1.540$, and the incident wavelength is $\lambda = 0.7\ \mu$m. The simulation parameters follow [35], where the waveguide samples can be fabricated via direct laser writing using a commercial Nanoscribe system and the photoresist IP-Dip. The effective refractive indices of

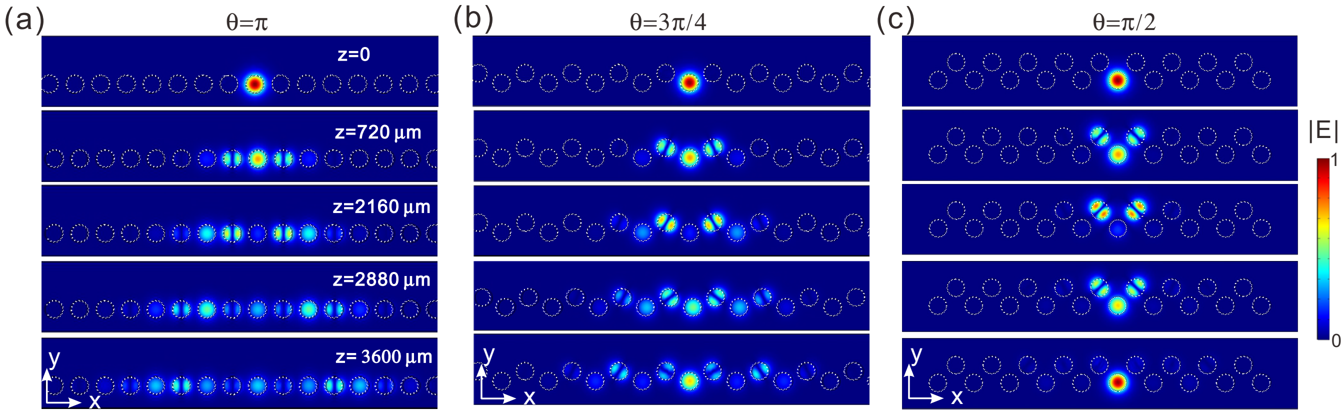

FIG. 3. Bulk dynamics for different central angle for (a) $\theta = \pi$, (b) $\theta = 3\pi/4$, and (c) $\theta = \pi/2$. In all cases, light is injected from a central waveguide with fundamental modes.

$l = 0$ and $l = 1$ modes are identical, with $n_{\text{eff0}} = 1.5424$. The waveguide separation is fixed at $d = 7\mu\text{m}$ for different central angles. Figure 2(b) show the band structures for $\theta = \pi$, $3\pi/4$, and $\pi/2$, respectively. The lines and dots represent theory and simulation results, demonstrating consistency. The energy E relates to effective refractive indices of supermodes n_{eff} as $E = (n_{\text{eff}} - n_{\text{eff0}})k_0$, where k_0 is the wave vector in vacuum and n_{eff0} is the effective refractive index for a single waveguide. As $\theta = \pi$, the two dispersive bands intersect at the center of the Brillouin zone. As $\theta = 3\pi/4$ and $\pi/2$, the three bands have gaps. As $\theta = \pi/2$, all three bands become dispersionless across the entire Brillouin zone, signifying the presence of AB caging, where the particles are expected to localize. By solving Eq. (2), the three eigenmodes are determined to be $\psi_2 = [0, -1, 1]$ and $\psi_{1,3} = [2, \pm 1, -1]$, with their distributions shown in the upper panel of Fig. 2(c). Simulated mode profiles (E_y) are present in the lower panel of Fig. 2(c). The $E_2 = 0$ band exhibits vanished fields at the $l = 0$ waveguide, while the $l = 1$ waveguide displays a p_y mode profile due to the superposition of two OAM modes. Furthermore, the field distributions for $E_{1,3} = \pm\sqrt{2}c$ bands also show a vertical p_y polarization at $l = 1$ waveguides, with opposite orientations for two bands, consistent with the theoretical expectations.

We further explore the bulk dynamics of wave propagation. Figures 3(a)–3(c) illustrate the simulated light propagation for three different central angles, with waves injected from a fundament waveguide situated in the middle of the structure. In general, a single injection induces the excitation of all Bloch modes at different momenta k. When $\theta = \pi$, corresponding to dispersive bands, light spreads, and a discrete diffraction pattern emerges during propagation, as depicted in Fig. 3(a). When $\theta = 3\pi/4$, while two bands are still curved, their slopes decrease, resulting in slower spreading, as shown in Fig. 3(b). Further reducing the central angle to $\theta = \pi/2$ causes all bands to become flat, leading to the localization of light without spreading. In Fig. 3(c), the waves are confined to the incident waveguide and its two neighboring waveguides due to destructive interference. At the beating length $L_b = 2\pi/(E_1 - E_3) \approx 3600\mu\text{m}$, the waves completely return to the initial waveguide.

III. COMPACT TOPOLOGICAL EDGE MODES IN AB CAGE

The proposed AB cage represents a square-root topological insulator characterized by a nonquantized topological invariant, capable of hosting topological edge states [56,57]. Its topological origin is identified through a transformation to either a SSH model or a stub lattice [58,59]. Here, we mainly focus on the compact feature of edge modes, which are robust even in a small lattice. Figure 4(a) shows the open band spectrum as the central angle varies. Blue dots and red circles represent bulk and topological edge modes, respectively. For any given θ, two edge modes manifest in both upper and lower

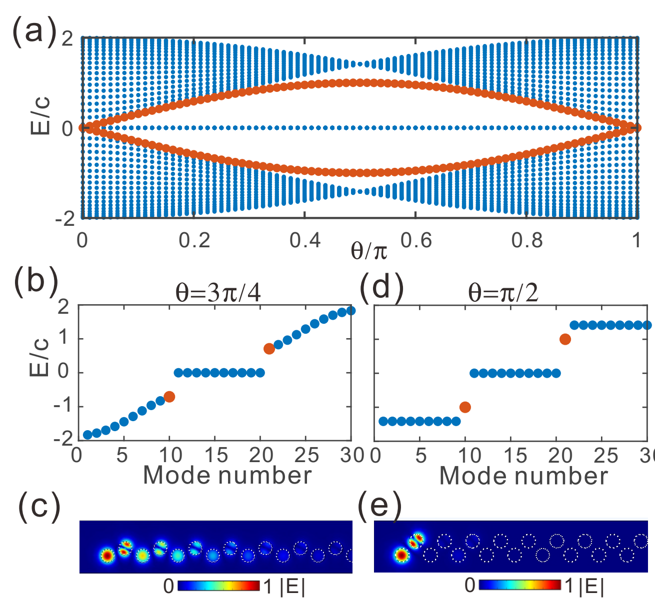

FIG. 4. Topological edge modes in finite zigzag waveguide arrays. (a) The energy spectra for a finite array. The red circles in the band gap indicate the topological edge modes. Panels (b) and (d) plot two energy spectra for $\theta = 3\pi/4$ and $\theta = \pi/2$, respectively. The red circles in the band gaps stand for topological edge modes. Panels (c) and (e) are the mode profiles for edge modes corresponding to (b) and (d), respectively.

band gaps, with energy given by

$$E_{\text{edge}} = \pm c \sin(\theta). \tag{7}$$

Their corresponding eigenstates are

$$\{a_n, b_n^+, b_n^-\} = \{\sqrt{2}, \pm 1, 1\}\delta^{n-1}, \quad \delta = -\frac{1 + e^{2i\theta}}{2}. \tag{8}$$

with $n < 1$ staring from the left boundary. Considering $|\delta| < 1$, the mode decays exponentially from the boundary into the bulk. Two central angles are chosen to analyze their bands and mode profiles. In Fig. 4(b), the open band spectrum for $\theta = 3\pi/4$ is displayed, showing two edge modes with $E = \pm c/\sqrt{2}$ in the gap. The corresponding simulated field distribution is shown in Fig. 4(c), localized at the left boundary and exhibiting an exponential decay away from it. Moving on to Fig. 4(d), the energy band for $\theta = \pi/2$ is presented, where bulk bands are flat, and two edge modes appear at the gap with $E_{\text{edge}} = \pm c$. The simulated fields in Fig. 4(e) are compact, confined to the left two waveguides. This compact feature can be strategically utilized to reduce the number of waveguide elements. We emphasize that the smallest lattice sites (a single plaquette) are achieved through perfect destructive interference. However, there is no strict necessity to limit the gauge flux to π since the lattice sites are reduced as the gauge flux approaches π. Therefore, the number of waveguides and gauge flux can be combined to optimize different application scenarios. In addition, the edge modes differ from compact bulk modes in two key aspects. First, their origins are different: one arises from a localized edge mode, while the other originates from bulk extended states. Consequently, the edge states benefit from topological protection. Second, the topological edge states exhibit better localization than bulk states. In the AB caging limit, the bulk modes become compactly localized but they are not robust against certain disorders and perturbations.

Topological edge modes arise from the nontrivial bulk of crystals, traditionally necessitating many lattice sites to hold their topological protection. Figure 5(a) illustrates the spectrum under open boundary condition as a function of the total number of array cells, with $\theta = 3\pi/4$. The edge modes are plotted in red. An additional site is introduced at the right edge, supporting an extra topological edge mode at the right boundary. In this configuration, the system has four edge modes within two gaps. For large cells, the eigenenergies of edge modes are degenerate in each gap. However, in smaller cells, degeneracy is lifted due to the mode coupling of the edge modes at different terminations, inevitably affecting their topological protection. This finite-size effect is attributed to their exponential decay feature. In contrast, for AB cages with $\theta = \pi/2$, the energy remains constant as the cell number decreases owing to their compact nature. Consequently, a topological waveguide array with only a few cells can be constructed based on AB cages. Wave propagation simulations are depicted in Figs. 5(c) and 5(d), utilizing only seven waveguides with light injected from the left edge. For $\theta = 3\pi/4$, light couples to the right boundary due to the overlap of edge modes. Conversely, for $\theta = \pi/2$, light remains confined to the left two waveguides due to their compact feature.

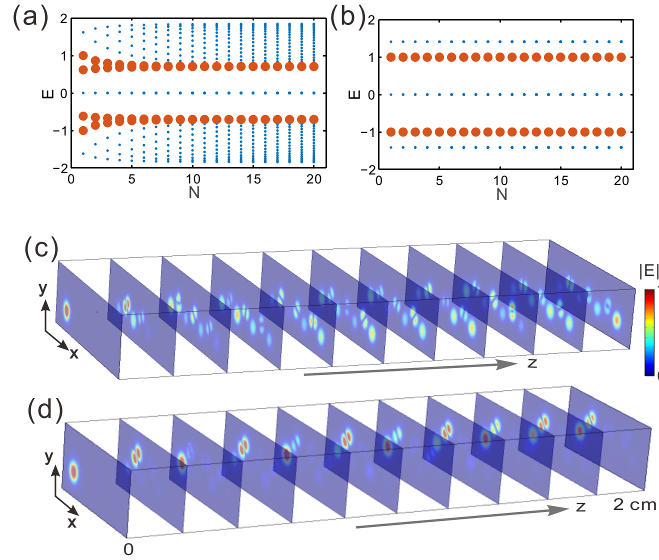

FIG. 5. Finite-size effect for topological edge modes. Panels (a) and (b) are the energy spectra versus the number of cells for $\theta = 3\pi/4$ and $\theta = \pi/2$, respectively. The bulk and edge modes are plotted in blue dots and red circles, respectively. Panels (c) and (d) are the light propagation for edge modes with $n = 3$ corresponding to $\theta = 3\pi/4$ and $\theta = \pi/2$, respectively. The edge modes for $\theta = \pi/2$ remain compact.

Topological edge modes are robust against certain disorders that do not break underlying symmetries, paving the way for disorder-insensitive photonic devices. The AB chains hold two nonsymmorphic symmetries described by

$$\prod H(k) \prod^{-1} = H^*(k),$$
$$\chi H(k) \chi^{-1} = -H^*(k), \tag{9}$$

with

$$\prod = \begin{pmatrix} 1 & 0 & 0 \\ 0 & e^{-i\phi/2}e^{-ikd} & 0 \\ 0 & 0 & e^{i\phi/2}e^{-ikd} \end{pmatrix},$$
$$\chi = \begin{pmatrix} 1 & 0 & 0 \\ 0 & -e^{-i\phi/2}e^{-ikd} & 0 \\ 0 & 0 & -e^{i\phi/2}e^{-ikd} \end{pmatrix}. \tag{10}$$

We consider three types of disorders, including on-site potential V_n at OAM_0 waveguides, complex coupling α_n between $\text{OAM}_{\pm 1}$ modes, and the coexistence of both. The inset in Fig. 6(a) depicts these disorders. In practical experiment, tuning the radius or refractive index of the waveguide core can control on-site potential V_n, breaking χ while preserving Π. The coupling α_n can be realized using elliptical waveguides, where the rotation angle introduces nonreciprocal phase factors and thus complex coupling [38]. Therefore, the proposed orbital waveguides provide a suitable platform to explore the robustness of AB cages. Real-valued α_n just breaks Π but preserves χ symmetry. The combination of V_n and complex α_n creates a general disorder that breaks both symmetries. We focus on the AB caging case with a central angle $\theta = \pi/2$,

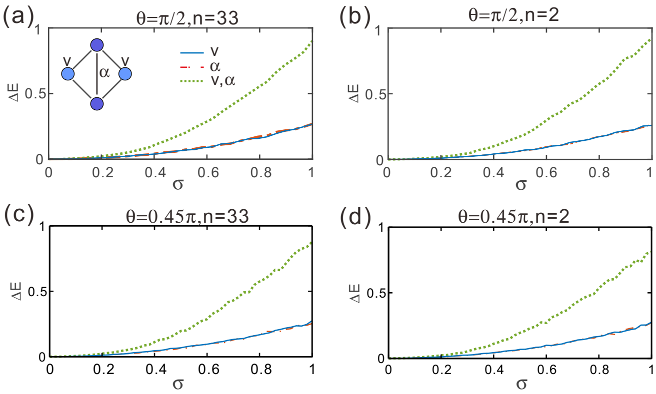

FIG. 6. Disorder analysis. Panels (a) and (b) are for the long chain and small chain in AB cages. Panels (c) and (d) are for $\theta = 0.45$. Three different disorders are considered, including the presence of only on-site potential (blue solid line), only additional coupling (red dash-dotted line), and both (green dashed line).

where the edge modes appear at $E = \pm c$. The robustness of the edge mode is characterized by the average mean squared difference $\Delta E/c = \langle |E_{\text{edge}}/c - 1\rangle$. All disorders are assumed to follow a Gaussian distribution with zero mean value, that is, $\langle a_n\rangle = \langle V_n\rangle = 0$. The standard deviation is denoted by σ. Figures 6(a) and 6(b) present the averaged mean squared difference of the edge modes for a long chain ($n = 33$) and a small chain ($n = 2$), respectively. Each point represents the average value calculated over 1000 iterations. When introducing on-site disorder or purely real coupling, the energy offset gradually increases with the increase of disorder strength, indicated by the blue solid lines and red dash-dotted lines. In contrast, the green dashed line represents the result of general disorder as the complex coupling α_n and V_n are both present. They follow a normal distribution with expected values $\langle \mathrm{Im}(\alpha_n)\rangle = \langle \mathrm{Re}(\alpha_n)\rangle = \langle V_n\rangle = 0$ and the same standard deviation σ. It exhibits a rapid increase with σ, indicating that the system is not robust against this kind of disorder. Notably, the disorder analysis for the small chain is similar to that of the long chain, suggesting that topological edge modes in AB cages remain robust irrespective of the number of waveguide elements. The discussion about disorder aims to identify which type of disorder the system performs better against. With symmetry-preserved disorder, the topological edge modes demonstrate stable eigenvalues and eigenstates. We also analyze the imperfect AB caging with $\theta = 0.45\pi$, as shown in Figs. 6(c) and 6(d). Nevertheless, their energy remains robust against the disorders in the on-site term V and coupling α, which indicates that the flux can be shifted without the requirement to stay exactly at π.

IV. ORBITAL HYBRIDIZATION FOR HIGH-ORDER OAM MODES

The hybrid coupling between OAM_0 and high-order OAM modes can also induce arbitrary gauge fluxes. As an example, we analyze the interaction between OAM_0 and $\text{OAM}_{\pm 2}$ modes. Considering that $\text{OAM}_{\pm 2}$ modes can be synthesized by d orbital modes, we consider a unit cell of a zigzag chain

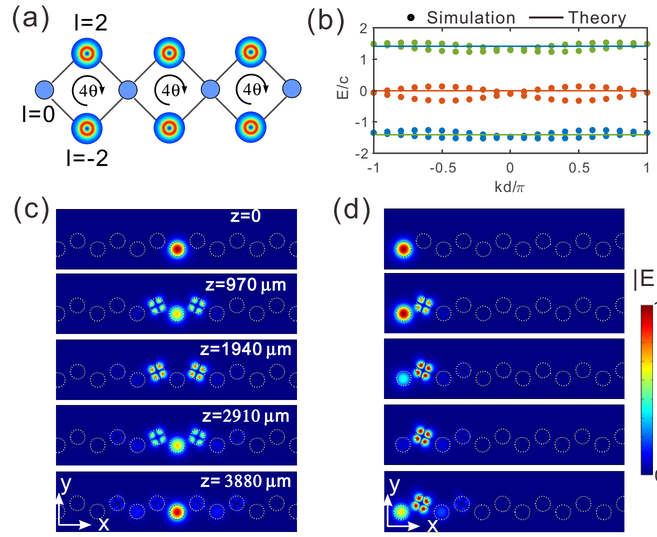

FIG. 7. Gauge flux induced by hybrid coupling between fundamental and high-order OAM modes. (a) Tight-binding lattice for coupling of $l = 0$ and $l = 2$ OAM modes. (b) Band structure for AB caging as central angle $\theta = 3\pi/4$. Panels (c) and (d) are the bulk and edge dynamics, respectively.

and formulate the Hamiltonian based on $s - d$ interaction,

$$H_{sd} = c\begin{pmatrix} 0 & \cos\theta & -\sin\theta & 0 \\ \cos\theta & 0 & 0 & \cos\theta \\ -\sin\theta & 0 & 0 & \sin\theta \\ 0 & \cos\theta & \sin\theta & 0 \end{pmatrix}. \tag{11}$$

Here, the $\text{OAM}_{\pm 2}$ modes are constructed using two d orbital modes with a phase difference of $\pi/2$. The transfer matrix T_2 is analogous to Eq. (6), leading to the Hamiltonian in the OAM basis,

$$H_{\text{OAM}} = T_2 H_{sd} T_2^{-1} = \frac{c}{\sqrt{2}}\begin{pmatrix} 0 & e^{i\theta} & e^{-i\theta} & 0 \\ e^{-i\theta} & 0 & 0 & e^{i\theta} \\ e^{i\theta} & 0 & 0 & e^{-i\theta} \\ 0 & e^{-i\theta} & e^{i\theta} & 0 \end{pmatrix}. \tag{12}$$

A nonreciprocal phase θ appears in the coupling term, twice that for $\text{OAM}_{\pm 1}$ modes. Consequently, the gauge flux threading each plaquette is $\phi = 4\theta$.

The effective tight-binding lattice for the coupling module for $\text{OAM}_{\pm 2}$ modes is depicted in Fig. 7(a). The condition for the AB caging effect is $4\theta = \pi + 2m\pi$ with m an integer. Considering that θ is in the range of 0 and π, the central angle can be $\theta = \pi/4$ or $3\pi/4$. However, when $\theta = \pi/4$, the next-nearest coupling between two adjacent waveguides becomes significant. Therefore, we choose $\theta = 3\pi/4$. The corresponding band structure under periodic boundary condition is shown in Fig. 7(b), with lines and dots representing theory and simulation, respectively. In the simulation, the refractive index of $\text{OAM}_{\pm 2}$ waveguide is $n_{\text{d}} = 1.5538$, ensuring the mode matching of OAM_0 and $\text{OAM}_{\pm 2}$ modes. Other parameters are the same as those used in Fig. 2. All three bands exhibit flatness across the entire Brillouin zone, signifying the AB caging effect. Further exploration of bulk dynamics involves injecting light from a $l = 0$ waveguide located at the structure center. The field distributions at different propagation distances are shown in Fig. 7(c). During the propagation, light gradually transfers into the two neighboring waveguides near the incident waveguides, and then returns to the initial waveguide, with a beating length $L_b = 2\pi/(E_3 - E_1) \approx 3880$μm. We also investigate the edge dynamics, as shown in Fig. 7(d). The waves concentrate at the two boundary waveguides during the propagation, corresponding to topological edge modes.

V. CONCLUSION

In conclusion, we have demonstrated the generation of arbitrary AGFs in an orbital zigzag waveguide array composed of two types of waveguide elements that support fundamental and first-order OAM modes, respectively. The orbital hybridization introduces complex coupling, leading to tunable AGFs controlled by the center angle of the zigzag chain. Specifically, when the central angle is set to $\pi/2$, an effective π gauge flux is induced, leading to AB caging effect characterized by flat bands and localized bulk modes. The topological edge modes in AB cages are shown to be compact, completely localized at the boundary waveguides, and robust against disorders preserving certain symmetries, even in relatively small lattices. The direct coupling scheme used in our approach eliminates the need for auxiliary waveguides, significantly reducing the total length of waveguide arrays along the propagation direction. Consequently, our proposed orbital hybridization is effective in miniaturizing the size of topological waveguide arrays. Furthermore, the mechanism is generalizable to high-order OAM modes. This alternative approach to orbital hybridization addresses challenges associated with arbitrary gauge fields in straight waveguides. It can be further applied to investigate other gauge-enriched topological phenomena, such as projective symmetry-protected topological phases [60,61], non-Hermitian physics [62,63], and high-order topological insulators [37,64].

ACKNOWLEDGMENT

The work was funded by the Scientific Research Project of Hubei University of Science and Technology (Grant No. BK302323)

[1] D. Tan, Z. Wang, B. Xu, and J. Qiu, Photonic circuits written by femtosecond laser in glass: improved fabrication and recent progress in photonic devices, Adv. Photonics **3**, 024002 (2021).

[2] T. Ozawa, H. M. Price, A. Amo, N. Goldman, M. Hafezi, L. Lu, M. C. Rechtsman, D. Schuster, J. Simon, O. Zilberberg, and I. Carusotto, Topological photonics, Rev. Mod. Phys. **91**, 015006 (2019).

[3] Z. Guo, Y. Wang, S. Ke, X. Su, J. Ren, and H. Chen, 1D photonic topological insulators composed of split ring resonators: a mini review, Adv. Phys. Res. **3**, 2300125 (2023).

[4] X.-X. Wang, Z. Guo, J. Song, H. Jiang, H. Chen, and X. Hu, Unique huygens-fresnel electromagnetic transportation of chiral Dirac wavelet in topological photonic crystal, Nat. Commun. **14**, 3040 (2023).

[5] L. Xie, L. Jin, and Z. Song, Antihelical edge states in two-dimensional photonic topological metals, Sci. Bull. **68**, 255 (2023).

[6] A. Li, W. Chen, H. Wei, G. Lu, A. Alù, C.-W. Qiu, and L. Chen, Riemann-encircling exceptional points for efficient asymmetric polarization-locked devices, Phys. Rev. Lett. **129**, 127401 (2022).

[7] A. Li, J. Dong, J. Wang, Z. Cheng, J. S. Ho, D. Zhang, J. Wen, X.-L. Zhang, C. T. Chan, A. Alù, C.-W. Qiu, and L. Chen, Hamiltonian hopping for efficient chiral mode switching in encircling exceptional points, Phys. Rev. Lett. **125**, 187403 (2020).

[8] M. Hafezi, E. A. Demler, M. D. Lukin, and J. M. Taylor, Robust optical delay lines with topological protection, Nat. Phys. **7**, 907 (2011).

[9] W. Song, W. Sun, C. Chen, Q. Song, S. Xiao, S. Zhu, and T. Li, Robust and broadband optical coupling by topological waveguide arrays, Laser Photonics Rev. **14**, 1900193 (2020).

[10] M. I. Shalaev, W. Walasik, A. Tsukernik, Y. Xu, and N. M. Litchinitser, Robust topologically protected transport in photonic crystals at telecommunication wavelengths, Nat. Nanotechnol. **14**, 31 (2019).

[11] M. A. Bandres, S. Wittek, G. Harari, M. Parto, J. Ren, M. Segev, D. N. Christodoulides, and M. Khajavikhan, Topological insulator laser: experiments, Science **359**, eaar4005 (2018).

[12] Q. Yan, B. Zhao, R. Zhou, R. Ma, Q. Lyu, S. Chu, X. Hu, and Q. Gong, Advances and applications on non-Hermitian topological photonics, Nanophotonics **12**, 2247 (2023).

[13] Z. Guo, X. Wu, S. Ke, L. Dong, F. Deng, H. Jiang, and H. Chen, Rotation controlled topological edge states in a trimer chain composed of meta-atoms, New J. Phys. **24**, 063001 (2022).

[14] J. Kang, R. Wei, Q. Zhang, and G. Dong, Topological photonic states in waveguide arrays, Adv. Phys. Res. **2**, 2200053 (2022).

[15] S. Shen, Y. V. Kartashov, Y. Li, and Y. Zhang, Floquet edge solitons in modulated trimer waveguide arrays, Phys. Rev. Appl. **20**, 014012 (2023).

[16] X. Shu, A. Li, G. Hu, J. Wang, A. Alù, and L. Chen, Fast encirclement of an exceptional point for highly efficient and compact chiral mode converters, Nat. Commun. **13**, 2123 (2022).

[17] Q. Cheng, Y. Pan, Q. Wang, T. Li, and S. Zhu, Topologically protected interface mode in plasmonic waveguide arrays, Laser Photonics Rev. **9**, 392 (2015).

[18] M. C. Rechtsman, J. M. Zeuner, Y. Plotnik, Y. Lumer, D. Podolsky, F. Dreisow, S. Nolte, M. Segev, and A. Szameit, Photonic floquet topological insulators, Nature (London) **496**, 196 (2013).

[19] S. Ke, W. Wen, D. Zhao, and Y. Wang, Floquet engineering of the non-Hermitian skin effect in photonic waveguide arrays, Phys. Rev. A **107**, 053508 (2023).

[20] Y. Li, C. Lu, S. Zhang, and Y.-C. Liu, Loss-induced floquet non-Hermitian skin effect, Phys. Rev. B **108**, L220301 (2023).

[21] A. El Hassan, F. K. Kunst, A. Moritz, G. Andler, E. J. Bergholtz, and M. Bourennane, Corner states of light in photonic waveguides, Nat. Photonics **13**, 697 (2019).

[22] T. Liu, K. Bai, Y. Zhang, D. Wan, Y. Lai, C. T. Chan, and M. Xiao, Finite barrier bound state, Light Sci. Appl. **13**, 69 (2024).
[23] S. Xia, Y. Liang, L. Tang, D. Song, J. Xu, and Z. Chen, Photonic realization of a generic type of graphene edge states exhibiting topological flat band, Phys. Rev. Lett. **131**, 013804 (2023).
[24] W. Song, W. Sun, C. Chen, Q. Song, S. Xiao, S. Zhu, and T. Li, Breakup and recovery of topological zero modes in finite non-Hermitian optical lattices, Phys. Rev. Lett. **123**, 165701 (2019).
[25] W. Wang, X. Wang, and G. Ma, Non-Hermitian morphing of topological modes, Nature (London) **608**, 50 (2022).
[26] M. Aidelsburger, S. Nascimbene, and N. Goldman, Artificial gauge fields in materials and engineered systems, C. R. Phys. **19**, 394 (2018).
[27] L. Yuan, Y. Shi, and S. Fan, Photonic gauge potential in a system with a synthetic frequency dimension, Opt. Lett. **41**, 741 (2016).
[28] C. Qin, F. Zhou, Y. Peng, D. Sounas, X. Zhu, B. Wang, J. Dong, X. Zhang, A. Alù, and P. Lu, Spectrum control through discrete frequency diffraction in the presence of photonic gauge potentials, Phys. Rev. Lett. **120**, 133901 (2018).
[29] S. Longhi, Aharonov–bohm photonic cages in waveguide and coupled resonator lattices by synthetic magnetic fields, Opt. Lett. **39**, 5892 (2014).
[30] S. Wang, C. Qin, W. Liu, B. Wang, F. Zhou, H. Ye, L. Zhao, J. Dong, X. Zhang, S. Longhi, and P. Lu, High-order dynamic localization and tunable temporal cloaking in ac-electric-field driven synthetic lattices, Nat. Commun. **13**, 7653 (2022).
[31] K. Fang, Z. Yu, and S. Fan, Photonic Aharonov-Bohm effect based on dynamic modulation, Phys. Rev. Lett. **108**, 153901 (2012).
[32] M. Hafezi, S. Mittal, J. Fan, A. Migdall, and J. M. Taylor, Imaging topological edge states in silicon photonics, Nat. Photonics **7**, 1001 (2013).
[33] Z. Liu, G. Wei, H. Wu, and J.-J. Xiao, Möbius edge band and Weyl-like semimetal flat-band in topological photonic waveguide array by synthetic gauge flux, Nanophotonics **12**, 3481 (2023).
[34] G. Cáceres-Aravena, D. Guzmán-Silva, I. Salinas, and R. A. Vicencio, Controlled transport based on multiorbital Aharonov-Bohm photonic caging, Phys. Rev. Lett. **128**, 256602 (2022).
[35] C. Jörg, G. Queraltó, M. Kremer, G. Pelegrí, J. Schulz, A. Szameit, G. von Freymann, J. Mompart, and V. Ahufinger, Artificial gauge field switching using orbital angular momentum modes in optical waveguides, Light Sci. Appl. **9**, 150 (2020).
[36] C. Jiang, Y. Song, X. Li, P. Lu, and S. Ke, Photonic möbius topological insulator from projective symmetry in multiorbital waveguides, Opt. Lett. **48**, 2337 (2023).
[37] J. Schulz, J. Noh, W. A. Benalcazar, G. Bahl, and G. von Freymann, Photonic quadrupole topological insulator using orbital-induced synthetic flux, Nat. Commun. **13**, 6597 (2022).
[38] C. Jiang, Y. Wu, M. Qin, and S. Ke, Topological bound modes with orbital angular momentum in optical waveguide arrays, J. Light. Technol. **41**, 2205 (2023).
[39] F. Gao, X. Xiang, Y.-G. Peng, X. Ni, Q.-L. Sun, S. Yves, X.-F. Zhu, and A. Alù, Orbital topological edge states and phase transitions in one-dimensional acoustic resonator chains, Nat. Commun. **14**, 8162 (2023).
[40] R. S. Savelev and M. A. Gorlach, Topological states in arrays of optical waveguides engineered via mode interference, Phys. Rev. B **102**, 161112(R) (2020).
[41] A. M. Marques, J. Mögerle, G. Pelegrí, S. Flannigan, R. G. Dias, and A. J. Daley, Kaleidoscopes of hofstadter butterflies and Aharonov-Bohm caging from 2 n -root topology in decorated square lattices, Phys. Rev. Res. **5**, 023110 (2023).
[42] J. Vidal, R. Mosseri, and B. Douçot, Aharonov-Bohm cages in two-dimensional structures, Phys. Rev. Lett. **81**, 5888 (1998).
[43] S. M. Zhang and L. Jin, Compact localized states and localization dynamics in the dice lattice, Phys. Rev. B **102**, 054301 (2020).
[44] S. M. Zhang, H. S. Xu, and L. Jin, Tunable Aharonov-Bohm cages through anti-$\mathscr{PT}$-symmetric imaginary couplings, Phys. Rev. A **108**, 023518 (2023).
[45] A. M. Marques, L. Madail, and R. G. Dias, One-dimensional 2^n-root topological insulators and superconductors, Phys. Rev. B **103**, 235425 (2021).
[46] F. Gao, Y.-G. Peng, Q.-L. Sun, X. Xiang, C. Zheng, and X.-F. Zhu, Topological acoustics with orbital-dependent gauge fields, Phys. Rev. Appl. **20**, 064036 (2023).
[47] A. O. Mikhin, V. Rutckaia, R. S. Savelev, I. S. Sinev, A. Alù, and M. A. Gorlach, Coherent control of topological states in an integrated waveguide lattice, Nano Letters **23**, 2094 (2023).
[48] M. Ehrhardt, S. Weidemann, L. J. Maczewsky, M. Heinrich, and A. Szameit, A perspective on synthetic dimensions in photonics, Laser Photonics Rev. **17**, 2200518 (2023).
[49] M. Yang, H.-Q. Zhang, Y.-W. Liao, Z.-H. Liu, Z.-W. Zhou, X.-X. Zhou, J.-S. Xu, Y.-J. Han, C.-F. Li, and G.-C. Guo, Realization of exceptional points along a synthetic orbital angular momentum dimension, Sci. Adv. **9**, eabp8943 (2023).
[50] L. Yuan, Q. Lin, A. Zhang, M. Xiao, X. Chen, and S. Fan, Photonic gauge potential in one cavity with synthetic frequency and orbital angular momentum dimensions, Phys. Rev. Lett. **122**, 083903 (2019).
[51] L. Allen, M. W. Beijersbergen, R. J. C. Spreeuw, and J. P. Woerdman, Orbital angular momentum of light and the transformation of Laguerre-Gaussian laser modes, Phys. Rev. A **45**, 8185 (1992).
[52] A. Turpin, G. Pelegrí, J. Polo, J. Mompart, and V. Ahufinger, Engineering of orbital angular momentum supermodes in coupled optical waveguides, Sci. Rep. **7**, 44057 (2017).
[53] T. Wen, S. Gao, W. Li, J. Tu, J. Li, Y. Xiao, H. Gao, Y. Chen, J. Zhao, C. Du, W. Liu, and Z. Li, Orbital angular momentum mode-multiplexed amplification and transmission based on a ring-core erbium-doped fiber, J. Light. Technol. **41**, 2116 (2023).
[54] G. Pelegrí, A. M. Marques, V. Ahufinger, J. Mompart, and R. G. Dias, Second-order topological corner states with ultracold atoms carrying orbital angular momentum in optical lattices, Phys. Rev. B **100**, 205109 (2019).
[55] J. Wang and X. Zhang, Orbital angular momentum in fibers, J. Light. Technol. **41**, 1934 (2023).
[56] M. Kremer, I. Petrides, E. Meyer, M. Heinrich, O. Zilberberg, and A. Szameit, A square-root topological insulator with non-quantized indices realized with photonic Aharonov-Bohm cages, Nat. Commun. **11**, 907 (2020).
[57] S. Mukherjee, M. Di Liberto, P. Öhberg, R. R. Thomson, and N. Goldman, Experimental observation of Aharonov-Bohm cages in photonic lattices, Phys. Rev. Lett. **121**, 075502 (2018).

[58] C. Martínez-Strasser, M. A. J. Herrera, A. García-Etxarri, G. Palumbo, F. K. Kunst, and D. Bercioux, Topological properties of a non-Hermitian quasi-1d chain with a flat band, Adv. Quantum Technol. **7**, 2300225 (2024).

[59] G. Cáceres-Aravena, B. Real, D. Guzmán-Silva, A. Amo, L. E. F. Foa Torres, and R. A. Vicencio, Experimental observation of edge states in SSH-Stub photonic lattices, Phys. Rev. Res. **4**, 013185 (2022).

[60] Z. Y. Chen, S. A. Yang, and Y. X. Zhao, Brillouin Klein bottle from artificial gauge fields, Nat. Commun. **13**, 2215 (2022).

[61] C.-A. Li, J. Sun, S.-B. Zhang, H. Guo, and B. Trauzettel, Klein-bottle quadrupole insulators and Dirac semimetals, Phys. Rev. B **108**, 235412 (2023).

[62] Z. Lin, L. Ding, S. Ke, and X. Li, Steering non-Hermitian skin modes by synthetic gauge fields in optical ring resonators, Opt. Lett. **46**, 3512 (2021).

[63] H. S. Xu and L. Jin, Pseudo-hermiticity protects the energy-difference conservation in the scattering, Phys. Rev. Res. **5**, L042005 (2023).

[64] M. Mazanov, A. S. Kupriianov, R. S. Savelev, Z. He, and M. A. Gorlach, Multipole higher-order topology in a multimode lattice, Phys. Rev. B **109**, L201122 (2024).